

Simulation of an extruded quadrupolar dielectrophoretic trap using meshfree approach

Cheng Xiang Song^{a,*}, Guirong Liu^a, Hua Li^b, Xu Han^c

^a*Center for Advanced Computations in Engineering Science (ACES), Department of Mechanical Engineering, The National University of Singapore, 10 Kent Ridge Crescent, Singapore 119260, Singapore*

^b*Institute of High Performance Computing, 1 Science Park Road, #01-01, The Capricorn, Singapore Science Park II, Singapore 117528, Singapore*

^c*College of Mechanical & Automotive Engineering, Hunan University, Changsha 410082, China*

Received 9 January 2006; accepted 17 March 2006

Available online 11 September 2006

Abstract

A numerical simulation of an extruded quadrupolar dielectrophoretic (DEP) trap is presented in this paper. To compute the electric field distribution of the trap, a meshfree collocation technique, termed as radial point collocation method (RPCM), is formulated. The simulation of the particle behaviors in the DEP trap is conducted by superimposing the DEP simulation results obtained using RPCM and the hydrodynamic results obtained using a commercial CFD package. The present model has been validated by experimental data and simulation results obtained using other numerical methods. The model is able to determine the full force field within the trap domain and to predict the trap strength under different electrode voltages. The present model has been used for parametric study of the extruded quadrupolar DEP trap. Meshfree technique used in this work has apparent advantages over traditional finite element method during the design optimization process because of the absence of remeshing.

© 2006 Elsevier Ltd. All rights reserved.

Keywords: Dielectrophoresis; Extruded quadrupolar trap; Meshfree method; Radial point collocation method; Collocation method

1. Introduction

As well known, when a neutral particle is suspended in non-uniform electric field, a dipole moment is induced on the particle. Since the electric field is non-uniform, two halves of the induced dipole experience two opposite forces with different magnitudes. This results in a net force, termed dielectrophoresis (DEP) [1,2]. As one of the attractive technologies for manipulating particles in micro-meter scale, DEP has a wide variety of applications in microelectromechanical system (MEMS), especially in biomedical field. In general, there are two main streams of DEP applications. One is microscale DEP separation systems and the other is microscale DEP traps.

Usually, there are mainly two techniques used in DEP separation systems. Based on the different electrical properties of the bio-particles, the first technique finds

operating conditions under which one subgroup of particles experience positive force, while the other subgroup of particles experience negative force, so separation could be achieved. Using this method, many types of particles have been separated. This type of separation includes separating Hela cells from normal human peripheral blood cells [3], human breast cancer cells from blood cells [4], viable from non-viable yeast [5], CD34+ cells from bone marrow samples and peripheral blood stem cells [6], and bacteria from blood cells [5,7]. Even smaller particles such as submicron latex sphere and virus could be separated using this method [8]. The other technique of separation is based on different DEP force magnitudes on different subgroups of particles due to the difference in particle radius or electrical properties. This technique could be used for separating polystyrene microbeads of different sizes [9], separating latex beads [10], performing differential analysis of human leukocyte [11], etc.

As the other type of DEP applications, DEP traps have been used in many areas, including particle capture [12],

*Corresponding author. Tel./fax: +65 6874 4795.

E-mail address: songchengxiang@nus.edu.sg (C.X. Song).

electrorotation [13], and force calibration of optical tweezers [14]. Early developments of DEP traps are meant to capture many particles at once, therefore, it is difficult to do quantitative analysis. Current cellular analysis requires single-particle manipulation. This type of applications enables one to expose cells to stimulus after they are trapped, then monitor the dynamic response of the cells individually, and sort them according to the dynamic response. This leads to the need to develop DEP-based systems that enable precise single-particle handling and manipulations. Most common electrode configurations developed previously were planar quadrupole trap [15] and the octopole field cage [16]. Planar quadrupole traps do not have strong-enough holding force against practical flow, while the octopole field cages are difficult to fabricate. It is noted that one of the most sophisticated designs is the extruded quadrupole trap developed by Voldman's group [17]. It can solve some of the problems. It has shown a stronger holding characteristic against practical flow and is more suitable for batch fabrication.

The aim of this work is to develop a numerical model for simulating the extruded quadrupole trap using a meshfree method [18]. In general, meshfree methods have superior advantages over traditional numerical techniques such as finite difference method (FDM) and finite element method (FEM) in terms of flexibility and convergence rate. Many meshfree schemes have been developed so far and achieved remarkable progress as summarized in [18]. One of such a method is the radial point interpolation method (RPIM) [18,27–36] based on different weakforms for different problems using local nodes and radial basis functions (RBFs). RBFs were used by Kansa as early as in 1990 for solving PDEs using all the nodes scattered in the problem domain [19,20]. In Kansa's work all the nodes in the problem domain were used. In this paper, a meshfree collocation method is formulated for DEP force field simulation using shape functions created using the radial point interpolation procedure based on local nodes and RBFs. Validity of this method is confirmed by comparing with both FEM and another meshfree method—weighted least-squares-based finite-difference scheme [21,22]. The simulation results have also been compared with experimental data extracted from Voldman's work [17]. Good agreement has been observed.

2. Theory and methodology

In this session, background information is given on the DEP theory, and the meshfree method used in electric field simulation. The governing equation for the electric field and its dimensionless form are also discussed in this session.

2.1. DEP theory

DEP is defined as the lateral motion imparted on uncharged particles as a result of polarization induced by

non-uniform electric fields. The induced dipole moment is subjected to a DEP force. For an isotropic and homogeneous dielectric spherical particle, the DEP force can be approximated by [1]

$$F_{DEP} = 2\pi\epsilon_m a^3 \text{Re}(f_{CM}) \nabla E_{rms}^2, \quad (1)$$

where ϵ_m is the permittivity of surrounding medium, a is the radius of the particle, E_{rms} is the root-mean-square magnitude of the electric field and it is a function of position. Re denotes the real part. f_{CM} is called the Clausius–Mossotti (CM) factor. For a homogeneous spherical particle, f_{CM} is given by [2]

$$f_{CM} = \frac{\epsilon_p - \epsilon_m}{\epsilon_p + 2\epsilon_m}, \quad (2)$$

where ϵ_p and ϵ_m are the complex permittivity of the particle and surrounding medium, respectively. They are given in the forms of $\epsilon_p = \epsilon_p + \sigma_p/j\omega$ and $\epsilon_m = \epsilon_m + \sigma_m/j\omega$, where ϵ_p , ϵ_m are the permittivity of particle and medium, and σ_p , σ_m are the conductivities of the particle and medium.

The sign of $\text{Re}(f_{CM})$ determines the particle experiencing positive or negative DEP force. When $\text{Re}(f_{CM}) > 0$, DEP force is aligned with the increasing direction of the electric field intensity and then the particle is attracted to electric field intensity maxima. When $\text{Re}(f_{CM}) < 0$, DEP force is aligned with the decreasing direction of the electric field intensity and then the particle is attracted to electric field intensity minima.

2.2. Governing equation

The whole simulation process is divided into the process of electric field simulation and the process of fluid velocity field simulation. The electric field simulation is done by using the meshfree code developed in our work, while the fluid velocity field simulation is done by using the commercial software. Therefore the only governing equation we are concerned of is the governing equation for the electric field.

For a homogeneous medium, the electric field can be determined by solving the Laplace equation of the electric potential, which is derived from the quasi-electrostatic form of Maxwell's equations [23]. In two-dimensional case, it can be written as

$$\frac{\partial^2 \psi}{\partial x^2} + \frac{\partial^2 \psi}{\partial y^2} = 0. \quad (3)$$

For mathematical simplicity and computational efficiency, non-dimensional formulation is introduced in the present computational process. In this work, electric potential ψ is scaled by V_0 , which is magnitude of the imposed voltage on the electrodes. This gives a non-dimensional potential $\psi' = \psi/V_0$. The coordinates are also scaled by d , which is half of the trap width. This gives new non-dimensional coordinates as $x' = x/d$, and $y' = y/d$. Substituting these non-dimensional variables into the

original governing Eq. (3), we get:

$$\frac{V_0}{d^2} \left(\frac{\partial^2 \psi'}{\partial x^2} + \frac{\partial^2 \psi'}{\partial y^2} \right) = 0. \quad (4)$$

Therefore, the non-dimensional potential also satisfies Laplace equation.

$$\frac{\partial^2 \psi'}{\partial x^2} + \frac{\partial^2 \psi'}{\partial y^2} = 0. \quad (5)$$

2.3. Radial point collocation method (RPCM)

Using meshfree techniques, a problem domain can be generally represented by a set of scattered nodes within the domain and on its boundaries. Let us consider a field function $u(\mathbf{x})$ defined in the problem domain Ω . It is assumed here that the function value of $u(\mathbf{x})$ at a point \mathbf{x}_Q is influenced only by those at the surrounding nodes in its vicinity. The small domain formed by the surrounding nodes is called support domain. Fig. 1 illustrates the idea of support domain.

The fundamental idea of point interpolation is to obtain the approximation of function value near the point \mathbf{x}_Q , and to create shape functions by enforcing the interpolation function passing through the function values at each node within the local support domain.

Using radial point interpolation procedure, a field variable $u(\mathbf{x})$ at the point \mathbf{x}_Q can be approximated by (see, e.g. [18])

$$\begin{aligned} u^h(\mathbf{x}, \mathbf{x}_Q) &= \sum_{i=1}^n R_i(\mathbf{x}) a_i(\mathbf{x}_Q) + \sum_{j=1}^m p_j(\mathbf{x}) b_j(\mathbf{x}_Q) \\ &= \mathbf{R}^T(\mathbf{x}) \mathbf{a}(\mathbf{x}_Q) + \mathbf{p}^T(\mathbf{x}) \mathbf{b}(\mathbf{x}_Q), \end{aligned} \quad (6)$$

where $R_i(\mathbf{x})$ is a RBF, $p_j(\mathbf{x})$ is a polynomial basis function, n is the number of nodes in the local support domain, m is the number of polynomial basis functions, $a_i(\mathbf{x}_Q)$ and

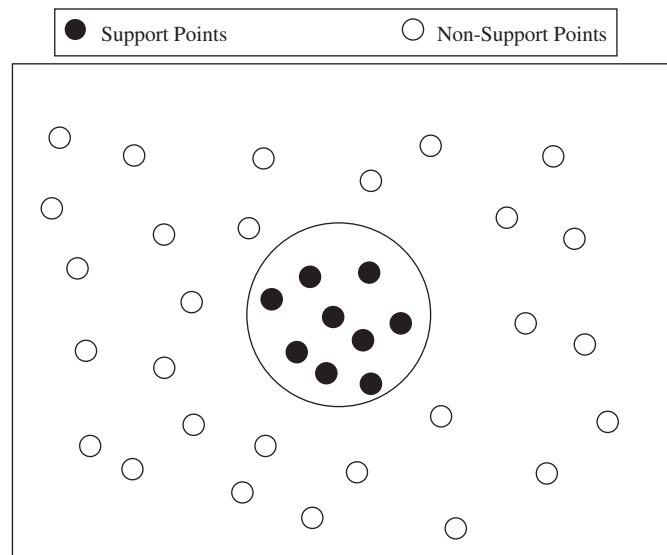


Fig. 1. Illustration of support domain.

$b_j(\mathbf{x}_Q)$ are the coefficients for the RBFs and polynomial basis functions corresponding to the interpolation point \mathbf{x}_Q , respectively.

There are many types of RBF that are used in the literature, and the characteristics of RBFs with arbitrary real parameters have been well investigated [18]. A number of typical RBFs with arbitrary real parameters are listed in Table 1. The multi-quadrics (MQ) radial basis interpolation function is used in this work and it can be given in the following form:

$$\begin{aligned} R_i(\mathbf{x}) &= R_i(x, y) = [(x - x_i)^2 + (y - y_i)^2 + (\alpha_c d_c)^2]^q \\ &= [r^2 + (\alpha_c d_c)^2]^q, \end{aligned} \quad (7)$$

where r is the distance between node \mathbf{x} and \mathbf{x}_i , d_c is a characteristic length, and α_c and q are two dimensionless shape parameters that can be adjusted in different problems for better performance. The detailed discussion of choosing proper shape parameters α_c and q is beyond the scope of this work, and can be found in [18]. According to the recommendation in [18], α_c is chosen between 1 and 2, and q is chosen to be 1.03 in this work. The adopted parameters have given stable solutions for the present work. d_c is usually the average spacing in the support domain, and in two-dimensional case it can be determined by

$$d_c = \frac{\sqrt{A_s}}{\sqrt{n} - 1}, \quad (8)$$

where A_s is an estimated area of the support domain, n is the number of nodes within the support domain.

To determine the coefficients $a_i(\mathbf{x}_Q)$ and $b_j(\mathbf{x}_Q)$, Eq. (6) are enforced to be satisfied at all n nodes in the local support domain. This leads to n linear equations, which can be written in matrix form as

$$\mathbf{U}_s = \mathbf{R}_Q \mathbf{a}(\mathbf{x}_Q) + \mathbf{P}_m \mathbf{b}(\mathbf{x}_Q), \quad (9)$$

where \mathbf{U}_s is the vector that contains all the field nodal variables in the support domain, and is in the form of

$$\mathbf{U}_s = \{u_1 \ u_2 \ \dots \ u_n\}^T. \quad (10)$$

The matrix of RBFs is in the form of

$$\mathbf{R}_Q = \begin{bmatrix} R_1(r_1) & R_2(r_1) & \dots & R_n(r_1) \\ R_1(r_2) & R_2(r_2) & \dots & R_n(r_2) \\ \vdots & \vdots & \ddots & \vdots \\ R_1(r_n) & R_2(r_n) & \dots & R_n(r_n) \end{bmatrix}. \quad (11)$$

Table 1
Typical radial basis functions with dimensionless shape parameters

Type	Expression	Dimensionless parameter
Multi-quadrics (MQ)	$R_i(x, y) = (r_i^2 + (\alpha_c d_c)^2)^q$	α_c, q
Gaussian (EXP)	$R_i(x, y) = \exp(-cr_i^2)$	c
Thin plate spline (TPS)	$R_i(x, y) = r_i^\eta$	η
Logarithmic RBF	$R_i(x, y) = r_i^\eta \log r_i$	η

The polynomial matrix is

$$\mathbf{P}_m^T = \begin{bmatrix} 1 & 1 & \cdots & 1 \\ x_1 & x_2 & \cdots & x_3 \\ y_1 & y_2 & \cdots & y_3 \\ \vdots & \vdots & \ddots & \vdots \\ p_m(x_1) & p_m(x_1) & \cdots & p_m(x_1) \end{bmatrix}. \quad (12)$$

The vector of coefficients for RBFs is

$$\mathbf{a}^T(\mathbf{x}_Q) = \{a_1, a_2, a_3, \dots, a_n\}. \quad (13)$$

The vector of coefficients for polynomial is

$$\mathbf{b}^T(\mathbf{x}_Q) = \{b_1, b_2, b_3, \dots, b_m\}. \quad (14)$$

In Eq. (11), r_k in $R_i(r_k)$ can be defined as

$$r_k = [(x_k - x_i)^2 + (y_k - y_i)^2]^{1/2}, \quad (k = 1, 2, \dots, n). \quad (15)$$

It is obvious that in Eq. (9), there are $n+m$ variables but only n equations. To determine the unique approximation, extra constraints are added to the polynomial terms, and lead to the following m more equations.

$$\sum_{i=1}^n p_j(\mathbf{x}_i) a_i = \mathbf{P}_m^T \mathbf{a} = 0, \quad j = 1, 2, \dots, m. \quad (16)$$

Combing Eq. (9) and Eq. (16), we get the following set of equations:

$$\begin{bmatrix} \mathbf{R}_Q & \mathbf{P}_m \\ \mathbf{P}_m^T & 0 \end{bmatrix} \begin{bmatrix} \mathbf{a}(\mathbf{x}_Q) \\ \mathbf{b}(\mathbf{x}_Q) \end{bmatrix} = \begin{bmatrix} \mathbf{U}_S \\ 0 \end{bmatrix} = \mathbf{G}\mathbf{a}_0. \quad (17)$$

\mathbf{a} and \mathbf{b} can be solved from Eq. (17), and finally Eq. (6) can be written as

$$\mathbf{u}^h(\mathbf{x}) = \Phi(\mathbf{x})\mathbf{U}_S = \sum_{i=1}^n \phi_i(\mathbf{x})u_i, \quad (18)$$

where $\Phi(\mathbf{x})$ are the shape functions, and can be expressed as

$$\Phi(\mathbf{x}) = \{\phi_1(\mathbf{x}), \phi_2(\mathbf{x}), \dots, \phi_n(\mathbf{x})\}. \quad (19)$$

The derivatives of $u(\mathbf{x})$ can be easily obtained by differentiating Eq. (18), e.g. first-order derivatives can be expressed as

$$\mathbf{u}_{,k}^h(\mathbf{x}) = \Phi_{,k}(\mathbf{x})\mathbf{U}_S = \sum_{i=1}^n \phi_{i,k} u_i, \quad (20)$$

where k denotes either the coordinate x or y , a comma designates a partial differentiation with respect to the indicated spatial coordinate that follows.

3. The extruded quadruple trap

Simulation of the extruded quadruple trap is divided into two stages for computation of DEP force distribution and computation of hydrodynamic force distribution. The total force is obtained by summation of these two types of forces. It is assumed that the fluid motion due to

electrothermal effect can be ignored, and the velocity field of the fluid is independent of the electric field. Therefore, we have decoupled the electric field and the fluid field in our simulation.

3.1. Determination of DEP force

To calculate DEP force, the electric potential distribution has to be obtained by solving the Laplace's equation. The electrodes arrangement is shown in Figs. 2(a) [24] and (b). For the simulation presented in this paper, a negative 5 V potential is applied to the upper right and lower left electrodes, while the other two electrodes are given a positive 5 V potential. The irregular field nodes are generated using MFree2D[©] software developed by Liu et al. [25]. Fig. 3 shows the node distribution near the electrodes.

The boundary conditions for the electric field simulation are shown in Fig. 4. Dirichlet conditions $\psi = \pm 5$ V are applied to the four electrodes as shown. Due to the symmetric nature of the whole system shown in Fig. 2(a), each symmetric line is a zero potential line. The left and right edges of a single trap are both symmetric lines seen in the whole system. Therefore, the Dirichlet conditions $\psi = 0$ are applied to the left and the right boundaries. For the upper and lower boundaries, we make them sufficiently far away from the electrodes, thus Dirichlet conditions $\psi = 0$ can be applied.

RPCM is used to solve the Laplace's Eq. (3). Eq. (3) can be discretized by collocating the differential equation at each node in the computational domain, and expressed as

$$\left(\frac{\partial^2 \psi}{\partial x^2}\right)_0 + \left(\frac{\partial^2 \psi}{\partial y^2}\right)_0 = 0 \quad (21)$$

and using Eq. (20), each term in Eq. (21) can be expressed as

$$\left(\frac{\partial^2 \psi}{\partial x^2}\right)_0 = \sum_{i=1}^n \phi_{i,xx} \psi_i, \quad (22)$$

$$\left(\frac{\partial^2 \psi}{\partial y^2}\right)_0 = \sum_{i=1}^n \phi_{i,yy} \psi_i, \quad (23)$$

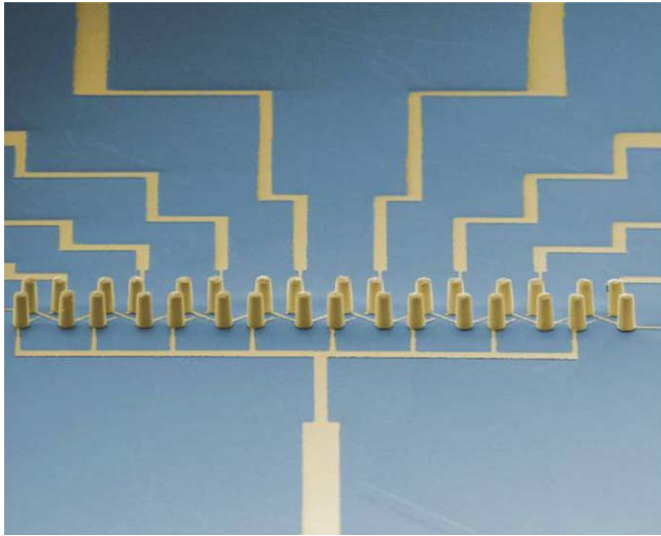
where u_i is the i th support node of reference node 0. Eq. (21) can then be written as

$$\sum_{i=1}^n \phi_{i,xx} \psi_i + \sum_{i=1}^n \phi_{i,yy} \psi_i = 0. \quad (24)$$

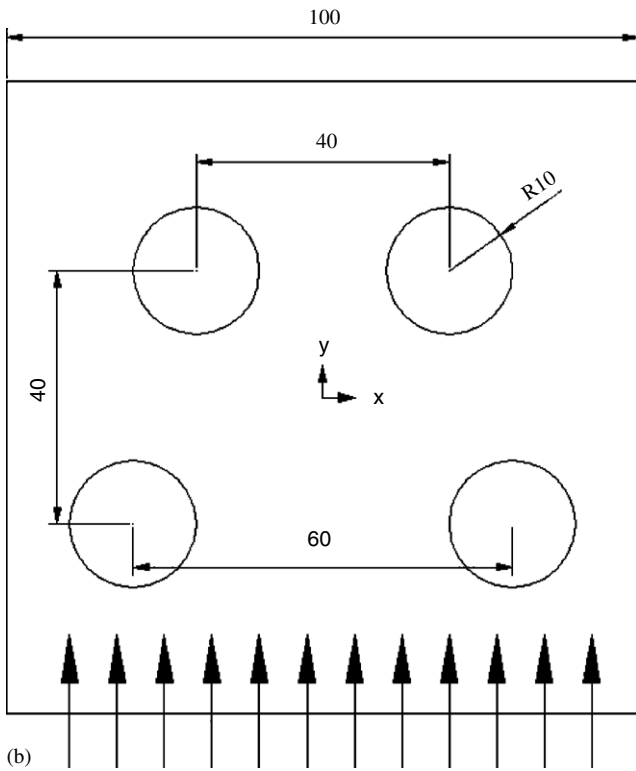
Eq. (24) is applied to every node within the computational domain, excluding the boundary nodes. In this problem, there are only Dirichlet boundary conditions; therefore, the following equation is applied to all the boundary nodes:

$$\psi_i = \bar{\psi}_i, \quad (25)$$

where $\bar{\psi}$ is the given electric potential on the boundary node i . With Eqs. (24) and (25), a set of algebraic equations



(a)



(b)

Fig. 2. (a) Extruded quadrupolar DEP trap; (b) Simulation domain for the simplified 2-D model.

can be expressed in the matrix form:

$$\mathbf{A} \cdot \boldsymbol{\psi} = \begin{bmatrix} a_{11} & a_{12} & \cdots & a_{1n} \\ a_{21} & a_{22} & \cdots & a_{2n} \\ & & \ddots & \\ a_{n1} & a_{n2} & \cdots & a_{nn} \end{bmatrix} \begin{bmatrix} \psi_1 \\ \psi_2 \\ \vdots \\ \psi_n \end{bmatrix} = 0, \quad (26)$$

where \mathbf{A} is the coefficient matrix. The electric potential distribution can be obtained by solving Eq. (26).

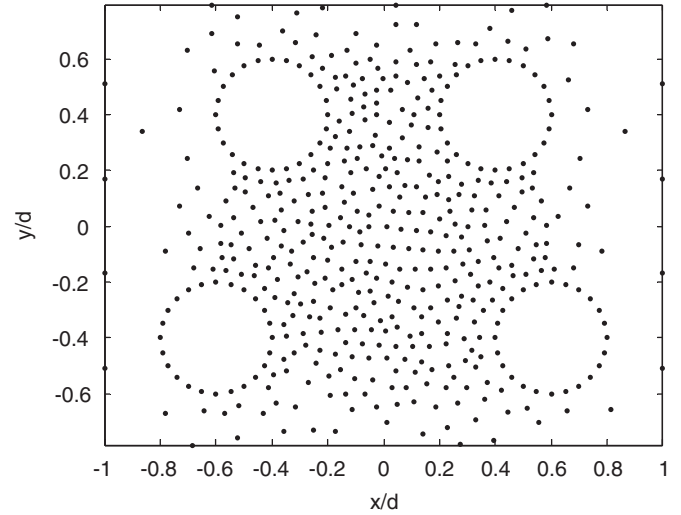


Fig. 3. Node distribution near the electrodes.

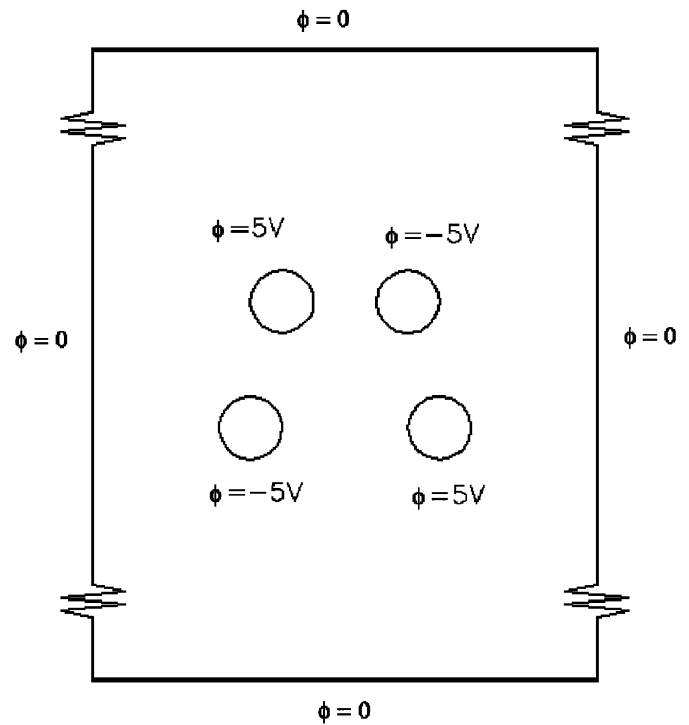


Fig. 4. Illustration of boundary conditions.

The next step is to determine the DEP force distribution using the relationship between electric potential and electric field intensity. The formula for DEP force is given in Eq. (1). Observing Eq. (1), only ∇E_{rms}^2 is related to the electric field, and it can be expressed as

$$\begin{aligned} \nabla E_{rms}^2 &= \nabla(E_x^2 + E_y^2) = \partial_x(E_x^2 + E_y^2)\mathbf{\hat{u}}_x \\ &+ \partial_y(E_x^2 + E_y^2)\mathbf{\hat{u}}_y = 2(E_x E_{xx} + E_y E_{yx})\mathbf{\hat{u}}_x \\ &+ 2(E_x E_{xy} + E_y E_{yy})\mathbf{\hat{u}}_y. \end{aligned} \quad (27)$$

All the other terms in Eq. (1) depend on material properties and thus we can group them as a constant term

G_{DEP} as

$$G_{DEP} = 2\pi\epsilon_m a^3 \text{Re}(f_{CM}). \quad (28)$$

If the DEP forces in x - and y -directions are denoted as $F_{DEP,x}$ and $F_{DEP,y}$, we have

$$F_{DEP,x} = 2G_{DEP}(E_x E_{xx} + E_y E_{yx}), \quad (29)$$

$$F_{DEP,y} = 2G_{DEP}(E_x E_{xy} + E_y E_{yy}). \quad (30)$$

Every term in Eqs. (29) and (30) can be expressed in terms of the electric potential by the following relations:

$$\begin{aligned} E_x &= -\frac{\partial\psi}{\partial x}, & E_y &= -\frac{\partial\psi}{\partial y}, & E_{xx} &= \frac{\partial E_x}{\partial x}, \\ E_{yy} &= \frac{\partial E_y}{\partial y}, & E_{xy} &= \frac{\partial E_x}{\partial y}, & E_{yx} &= \frac{\partial E_y}{\partial x}. \end{aligned} \quad (31)$$

If we define non-dimensional force components as

$$F'_{DEP,x} = \nabla E'^2_x, \quad F'_{DEP,y} = \nabla E'^2_y \quad (32)$$

by substituting the non-dimensional variables $\psi' = \psi/V_0$, $x' = x/d$, and $y' = y/d$ into Eqs. (29) and (30), we can obtain the relationship between non-dimensional and dimensional DEP force components as

$$F_{DEP,x} = G_{DEP} \frac{V_0^2}{d^3} F'_{DEP,x}, \quad F_{DEP,y} = G_{DEP} \frac{V_0^2}{d^3} F'_{DEP,y}. \quad (33)$$

3.2. Determination of hydrodynamic force

The above DEP force formulation enables us to determine the detailed information of both DEP force magnitudes as well as directions. The second part of the simulation process is to determine the drag force given by the medium at every point within the trap. To do this, we need a detailed simulation of the velocity field for the fluid flow. Commercial computational fluid dynamics (CFD) software Fluent[®] 6.0 is employed to perform the fluid simulation since it is available and convenient to use.

A particle in fluid experiences a drag force that can be approximated by Stoke's law as [26]

$$F_{Drag} = -fv, \quad (34)$$

where f is the friction factor of the particle and v is the particle velocity. The fluidic velocity field is obtained using Fluent[®] 6.0. For low Reynolds number, the friction factor for a spherical particle is given by

$$f = 6\pi\eta a, \quad (35)$$

where a is the hydrodynamic radius of the particle and η is the viscosity of the fluid medium.

3.3. Determination of the total resultant force

The above formulations give us both the DEP force F_{DEP} and the hydrodynamic force F_{Drag} at every position within the trap. We now have enough information to

determine the total resultant force. To do this, we simply need to add DEP force and hydrodynamic drag force in x - and y -directions, respectively at each of the field point.

$$F_{Total,x} = F_{DEP,x} + F_{Drag,x}, \quad (36)$$

$$F_{Total,y} = F_{DEP,y} + F_{Drag,y}. \quad (37)$$

Since the fluid field simulation and electric field simulation do not employ the same set of field notes, an interpolation procedure is necessary using RPCM before we can add these two fields together.

4. Model validation

To validate the accuracy and reliability of the present model, electric potential results obtained using RPCM are compared with the simulated results using least-squares-based finite-difference (LSFD) schemes. The final results are also compared with experimental data. The comparisons prove that the present model gives reasonably accurate and reliable results.

The simulations are carried out on polystyrene beads at a frequency 20 MHz. Bead's relative permittivity, and conductivity are 2.5, and 10^{-4} S/m, respectively. The fluid used for the simulations is physiological saline with conductivity of 1 S/m, and relative permittivity of 80. Unless noted otherwise, these properties are applicable to all simulations presented in this paper.

4.1. Comparison between RPCM and LSFD

RPCM results are compared with LSFD results using FEM results with high mesh density as the reference solution. The comparison is shown in Figs. 5 and 6. Fig. 5 shows that near the electrode posts, where the node distribution is very irregular, RPCM gives much better results than LSFD method. This proves the robustness and flexibility of RPCM. The relative error in Fig. 6 is computed based on the reference solution. It is observed from the figures that both the meshfree methods are convergent, and RPCM gives much more accurate results. The contour plot of the RPCM simulation of the electric potential is shown in Fig. 7.

4.2. Comparison between numerical prediction and experimental results

In order to further validate the accuracy of the model, comparisons are done between our numerical prediction and the experimental results. Experimental data is obtained from Voldman's paper [17], where the flowrate measurements were taken on average 4.3 times, and the experimental error was within 1 standard deviation. To make the data more comparable, the following modification is made. In actual fabrication, an interconnection at bottom of the trap is made between the posts that have same electric voltage. This is clearly shown in Fig. 2(a). It is shown in

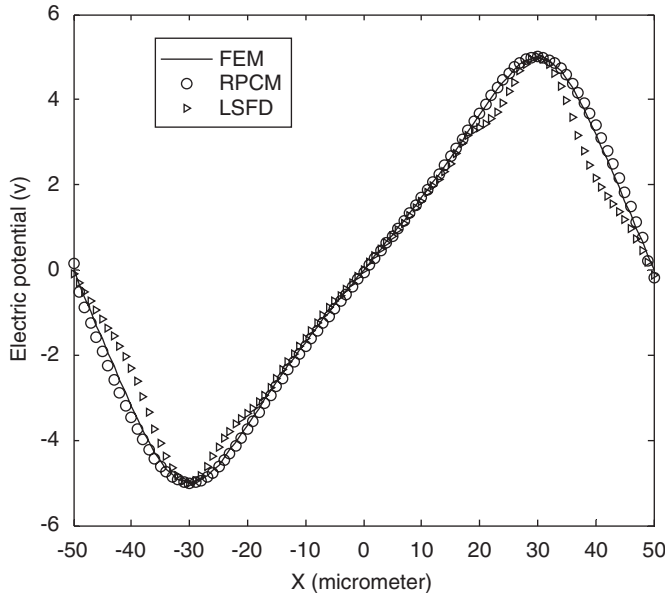


Fig. 5. Comparison of electric potential between RPCM and LSFD on line $y = -30$.

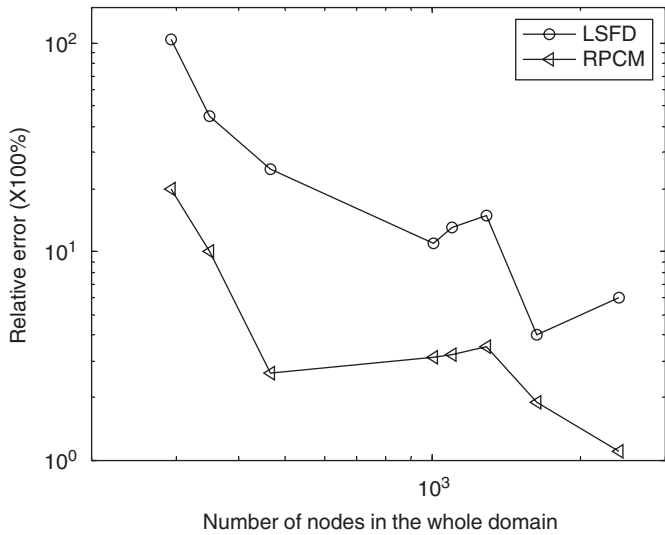


Fig. 6. Comparison of convergence between RPIM and LSFD.

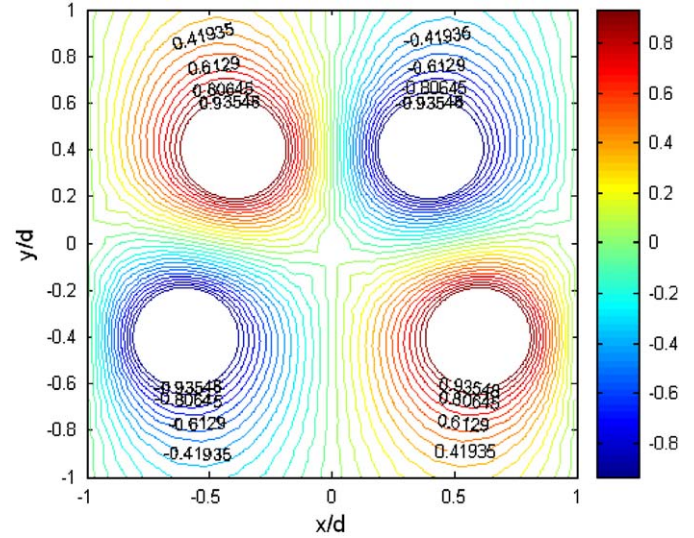


Fig. 7. Non-dimensional electric potential field obtained using RPCM.

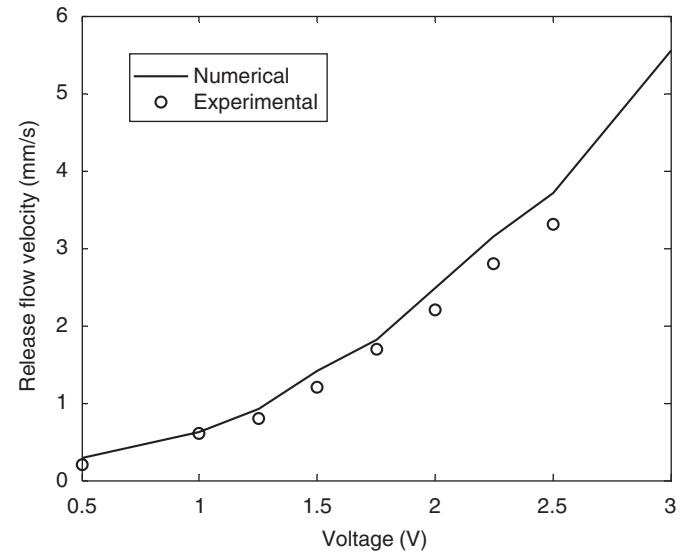


Fig. 8. Numerical and experimental results comparison for 13.2 μm diameter beads

Voldman's study [17] that trap with interconnection is weaker than trap without interconnection in terms of holding strength. It is observed that the difference is about a factor of 2.7. In the present 2-D simulation, the interconnection influence is neglected. We scale down the numerical results by a constant 2.7, and then do the comparisons with experimental data. It has been proved that this modification is reasonable, and we get close agreement with the experimental results.

The comparisons are shown in Figs. 8 and 9 for two different beads with diameters of 13.2 and 10.0 μm , respectively. The numerical predictions are done using the parameters described above, except that to be in

consistence with the experiment, fluid medium's conductivity of 0.01 S/m is used, bead conductivity of 2×10^{-4} S/m is used, and frequency used is 1 MHz. The comparisons with experimental data further validate the accuracy of the present model, and give us more confidence in the prediction results. If an average error is defined as

$$e = \sqrt{\frac{\sum (v_{exp} - v_{num})^2}{\sum v_{exp}^2}}, \quad (38)$$

where v_{exp} is the experimental result for release velocity and v_{num} is the numerical simulation result for release velocity. Figs. 8 and 9 illustrate that the average error is about 12.4% for 13.2 μm diameter beads, and the average error is about 13.3% for 10.0 μm diameter beads. This is acceptable

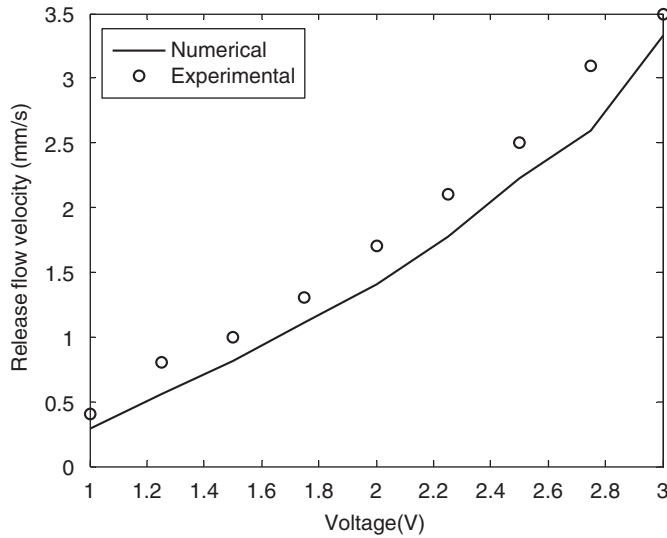


Fig. 9. Numerical and experimental results comparison for 10 μm diameter beads.

for practical application. It is observed that in Fig. 8, the numerical values are higher than experimental values, but in Fig. 9, the numerical values are lower than experimental values. This is due to experimental errors. The average errors for these two cases are quite close as mentioned above. The present model has been validated in predicting the performance of the extruded quadruple trap, and the accurate results strongly suggest it could be very useful for future DEP device design.

5. Results and discussion

5.1. Results for resultant force field

The total resultant force field is computed by superimposing the electric DEP force F_{DEP} and the hydrodynamic force F_{Drag} in x - and y -directions, respectively. Once the total force field is obtained, all the information can be obtained for analyzing the particle behavior in the trap. To examine the trap strength, release flow velocity is defined as the maximum flow velocity under which the trap can still hold the particle. Beyond this velocity, the particle will be released.

Fig. 10 demonstrates how to determine the release flow velocity. The particle used in this example has a radius of 6.25 μm , and the applied voltage is 5V. Due to the symmetric nature of the designed system, it is obvious that the balance point is always on vertical middle line. Fig. 10 shows vertical forces along this line at different flow velocities. Examining the curve for 1 mm/s flow velocity, there are two minimum points where the force is negative. The negative sign indicates that the force is in opposite direction of the flow. These two minima act as barriers to the particles. For the particles to escape from the trap, the barrier force has to be positive. As the velocity of the flow increases, the total forces increase, and the curve moves up.

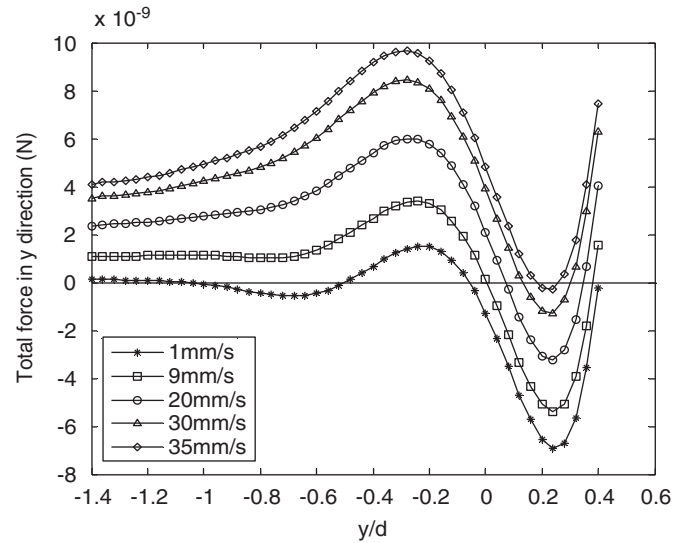


Fig. 10. Determination of release flow velocity.

Once the vertical force at every point on this line becomes positive, the particles will be released. The minimum flow velocity for the particles to be released is determined to be the release velocity. In this case, once the fluid velocity exceeds 35 mm/s, the trap is no longer able to hold the particles. Thus the release velocity is determined to be 35 mm/s.

From the curve at 1 mm/s in Fig. 10, it is noted that the first barrier prevents the loading of the particles, and the second barrier prevents the particles from escaping. Since forces around the first barrier are negative in this case, it is hard to load the particles. When the velocity increases, the first barrier becomes less obvious, and finally disappears. This means that there is a minimum velocity that should be fulfilled before the particles could be loaded. In this 2-D simulation, when the particles achieved static condition, they will stay at the equilibrium points, which are the intersections of the curves with zero force line. For the case of 1 mm/s flow velocity in Fig. 10, there are four equilibrium points. Once the velocity increases, the four equilibrium points reduce to two. As the velocity continues to increase, the two equilibrium points become closer and closer, and finally merges into one. This is the condition when the particles start to be released.

Fig. 11 illustrates the release flow velocity under different electrode voltages. The curve indicates the holding characteristic of the trap. The release flow velocity is one of the indicators of the trap strength. As expected, the higher the electrode potential is, the stronger the trap strength is. The characteristic curve shows a non-linear relationship between the voltage and the trap strength. The non-linear behavior can be predicted from Eq. (33), which shows DEP force is proportional to square of the electrode potential. Therefore after combining the effects of DEP force and the hydrodynamic force, Fig. 11 shows a higher gradient as the potential becomes larger.

5.2. Variation of holding characteristic with trap geometry

In order to investigate the influence of electrodes arrangement on the holding characteristics, Figs. 12–14 are plotted. Three parameters are investigated as listed in Table 2. They are the entrance posts separation L , exit posts separation W , and the trap length D . Our objective is to make the trap easy to load and have higher strength as well. Post radius is used as a reference dimension, and all other parameters are studied by changing the relative dimensions with respect to post radius.

The advantage of using meshfree technique is apparent during the parametric study process. In traditional finite element approach, remeshing process has to be done when each time the design parameters are changed. This is very tedious and time-consuming, especially, when the number of design parameters gets larger. While using meshfree method, we only need to redistribute the field nodes, and

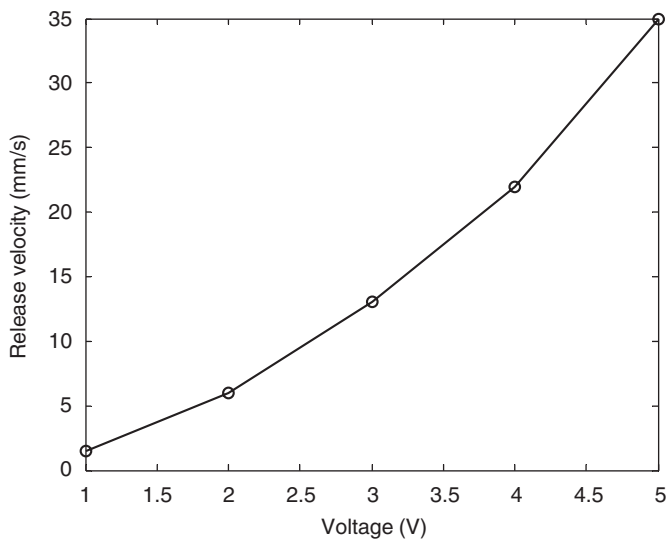


Fig. 11. Variation of release flow velocity with voltage.

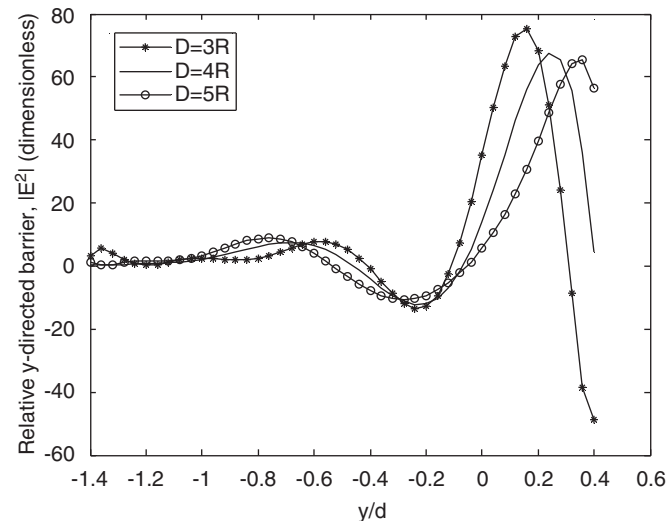


Fig. 12. Effect of trap length on strength of the trap.

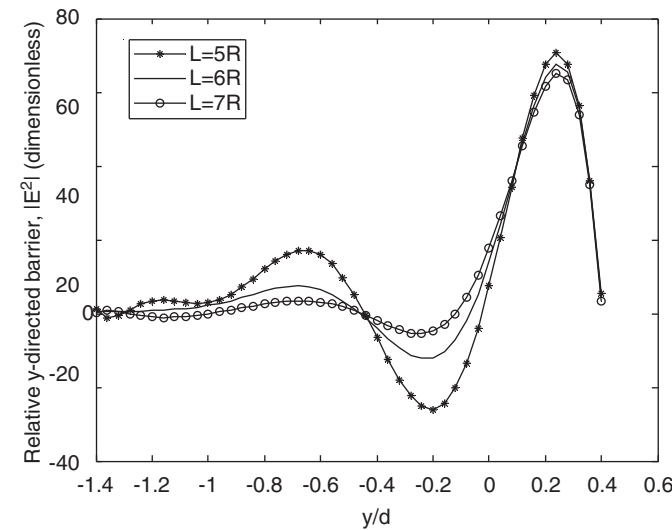


Fig. 13. Effect of entrance posts separation on strength of the trap.

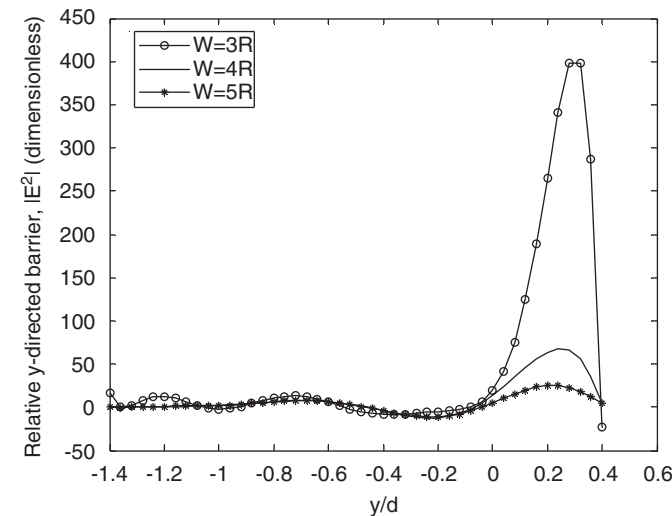
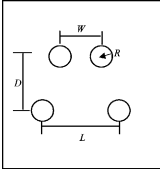


Fig. 14. Effect of exit posts separation on strength of the trap.

Table 2
Schematic of geometrical parameters ($R = 10\mu\text{m}$ is used as reference parameter)

Initial geometry	Parameters	Range of variation
	L	$5R, 6R, 7R$
	W	$3R, 4R, 5R$
	D	$3R, 4R, 5R$

the process is fast and easy. The following is the result of our parametric study using meshfree method.

Fig. 12 shows three characteristic curves of the trap with trap length varying from $3R$ to $5R$. The two maximum points on each curve are called entrance barrier and exit

barrier, respectively. The left maxima located around the entrance posts are entrance barriers, while the right maxima are the exit barriers. The magnitude of the entrance barrier represents the easiness of loading. It can be seen from the figure that the entrance barrier magnitudes for these three configurations are almost the same. This means that change of the trap length does not affect the loading very much. The magnitude of the exit barrier represents the easiness to escape for the particles; therefore it reflects the trap strength. The figure does not show much difference among these three configurations. Fig. 12 also shows that the locations of the entrance barriers and the exit barriers change in different configurations. This is because the locations of the posts are changing, and the barriers are always located near the posts. Another observation from this figure is that towards the left of the entrance barriers, the forces are almost identical for these three configurations. This is reasonable because the change of trap length has little effect on the flow before it enters the trap. Although the change of trap length has no or little effect on the trap strength and the loading, it should not be designed to be too small due to the restriction of particle size.

Fig. 13 demonstrates three characteristic curves of the trap with entrance posts separations varying from $5R$ to $7R$. It is known from the figure that change of the entrance posts separation will significantly affect the entrance barrier. For $5R$ separation, the entrance barrier is strongest, and therefore this configuration is the most difficult to load. The effect of entrance posts separation on the exit barrier is very little. The forces near the exit posts are very close for all the three configurations. It is clearly observed that the position of the barriers are almost identical for these three configurations, this is because the changes of locations of the posts only happens in the horizontal direction, therefore it could not be seen on the vertical middle line. Comparing Fig. 13 with Fig. 12, the effect on the entrance area due to change of entrance separation is more obvious. This is because the change of entrance separation has changed the electric distribution as well as the flow velocity near the entrance, but beyond $y/d = -1.4$, the effect decays fast, and little difference could be observed among these three configurations. It is also observed that the three configurations reduce to the same level beyond the exit barriers.

Fig. 14 shows three characteristic curves of the trap with exit posts separations varying from $3R$ to $5R$. As we can see, the exit barrier strength is extremely sensitive to the exit posts separation, thus it can be very effective to increase the trap strength by adjusting the separation of the exit posts. Strength for the $3R$ configuration has shown almost 8 times higher compared with $4R$ configuration. The entrance barriers have become very small compared with the exit barriers, and almost no difference in entrance barriers are observed among these configurations. It is also observed that beyond the exit barrier, all the three configurations almost come back to the same level.

5.3. Variation of holding characteristic with particle radius

Since both the DEP force and the hydrodynamic drag force are related to the particle radius a , the holding characteristic will vary with a . Theoretically, the DEP force increases faster than hydrodynamic drag force with increase of radius, because DEP force is proportional to R^3 , and drag force is proportional to R . Therefore the release flow velocity is expected to increase as the particle radius increases. Table 3 shows the present simulations for change of release flow velocity with particle radius at a voltage of 2 V. The results agree well with theoretical prediction. The DEP trap naturally has stronger holding force for larger particles, and greater flow velocity is necessary to release the particle. There is no simple direct relationship between the particle radius and the release flow velocity. As we can see from the figure, when radius changes from 6 to $7\mu\text{m}$, the release velocity almost doubles, but when radius change from 7 to $8\mu\text{m}$, the change in release velocity is only 0.5 mm/s. The relationship is fairly complicated, and this is mainly due to the complexity of the directions of the DEP force and hydrodynamic drag force. The general guideline is that the trap shows a stronger holding characteristic for larger particles of the same properties.

5.4. Variation of holding characteristic with Clausius–Mossotti factor

It is clearly shown in Eq. (2) that CM factor is related to frequency, and it is also the only frequency-dependent component in DEP force. Therefore, the frequency study here only focuses on CM factor. Fig. 15 shows the real part of CM factor of a $10\mu\text{m}$ diameter bead in two different fluid media. In high conductivity medium (0.01 S/m), the real part of CM factor does not vary too much with frequency, because CM factor is dominated by the high conductivity of the solution. In low-conductivity medium ($8.0 \times 10^{-4}\text{ S/m}$), the real part of CM factor increases in magnitude as frequency increases. It is concluded from the figure that at lower frequency, CM factor is sensitive to the solution conductivity, while it is insensitive at higher frequency. This understanding can help us to choose proper fluid and suitable frequency in the practical experimental situation.

As show in Eq. (1), the real part of CM factor is directly proportional to the DEP force; therefore, an increase in the real part of CM factor causes a corresponding increase in DEP force at the same voltage. Then a stronger holding characteristic is expected. This implies that in low-conductivity medium, the DEP force is very much

Table 3
Influence of particle radius on the release velocity

a (μm)	4	5	6	7	8	9
Release velocity (mm/s)	3	5.5	6	11	11.5	14

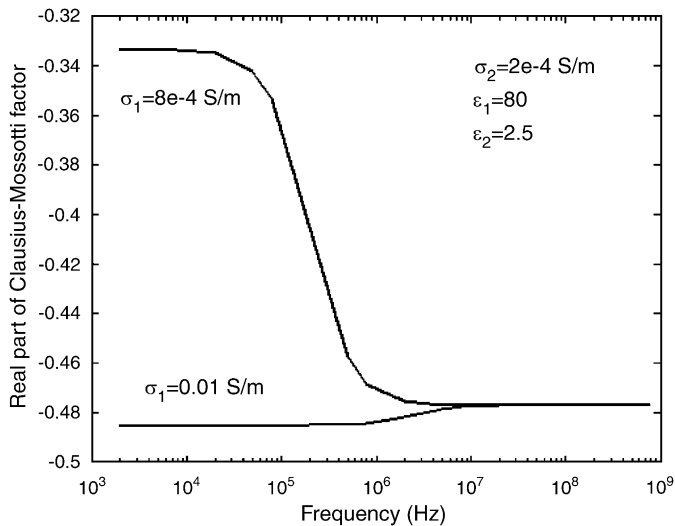


Fig. 15. Change of CM factor with frequency in different fluid.

dependent on the applied frequency. To achieve higher trap strength, a higher frequency is recommended. While if it is required to achieve higher strength at lower frequency, a high-conductivity medium should be considered.

6. Conclusion

The model developed in this work enables us to understand more detailed information on the behavior of the particles within the extruded quadrupolar trap. The simulation result by this model is expected to be close to the real situation. The model is able to approximate the strength of the trap, which is one of the main concerns in practical DEP device design. It can also be used for design optimization purpose. The meshfree RPCM method has been used for the simulation work. Numerical comparisons have shown that RPCM has superior advantage in terms of higher accuracy and flexibility. The trap strength can be determined under any electrode voltages. It has also been shown by comparing with experimental data that the model gives reasonable accuracy.

Compared with traditional FEM techniques, the mesh-free method employed here eliminates the remeshing process during design optimization process. This can significantly reduce the computational time and increases the flexibility. The meshfree technique can be used for simulations of different types of geometries and arbitrary configuration of electrodes. It can be potentially used to determine the optimal electrode configuration to maximize the dielectrophoresis effect.

The present model can be used for any DEP system designs, and more sophisticated model could be developed based on the present one. For instance, particle and particle interaction, change of fluid field due to the presence of particles, multipole DEP forces, could all be implemented into the model.

References

- [1] Pohl HA. Dielectrophoresis. Cambridge: Cambridge University Press; 1978.
- [2] Jones TB. Electromechanics of particles. Cambridge: Cambridge University Press; 1995.
- [3] Cheng J, Sheldon EL, Wu L, Heller MJ, O'Connell P. Isolation of cultured cervical carcinoma cells mixed with peripheral blood cells on a bioelectronic chip. *Anal Chem* 1998;70:2321–6.
- [4] Gascoyne PRC, Wang XB, Huang Y, Becker FF. Dielectrophoretic separation of cancer cells from blood. *IEEE Trans Ind Appl* 1997;33:670–8.
- [5] Wang XB, Huang Y, Burt JPH, Markx GH, Pethig R. Selective dielectrophoretic confinement of bioparticles in potential energy wells. *J Phys D (Appl Phys)* 1993;26:1278–85.
- [6] Talary MS, Mills KI, Hoy T, Burnett AK, Pethig R. Dielectrophoretic separation and enrichment of CD34+ cell subpopulation from bone marrow and peripheral blood stem cells. *Med Biol Eng Comput* 1995;33:235–7.
- [7] Cheng J, Sheldon EL, Wu L, Uribe A, Gerrue LO, Carrino J, et al. Preparation and hybridization analysis of DNA/RNA from *E. coli* on microfabricated bioelectronic chips. *Nat Biotechnol* 1998;16:541–6.
- [8] Green NG, Morgan H. Dielectrophoretic separation of nanoparticles. *J Phys D—Appl Phys* 1997;30:L41–4.
- [9] Wang XB, Vykoukal J, Becker FF, Gascoyne PRC. Separation of polystyrene microbeads using dielectrophoretic/gravitational field-flow-fractionation. *Biophys J* 1998;74:2689–701.
- [10] Markx GH, Pethig R, Rousselet J. The dielectrophoretic levitation of latex beads with reference to field-flow fractionation. *J Phys D (Appl Phys)* 1997;30:2470–7.
- [11] Yang J, Huang Y, Gascoyne PRC. Differential analysis of human leukocytes by dielectrophoretic field-flow-fractionation. *Biophys J* 2000;78:2680–9.
- [12] Green NG, Morgan H, Milner JJ. Manipulation and trapping of sub-micron bioparticles using dielectrophoresis. *J Biophys Methods* 1997;35:89–102.
- [13] Reichle C, Muller T, Schnelle T, Fuhr G. Electro-rotation in octopole micro cages. *J Phys D* 1999;32:2128–35.
- [14] Fuhr G, Schelle T, Muller T, Hitzler H, Monajembashi S, Creulich KO. Force measurement of optical tweezers in electro-optical cages. *Appl Phys A Mater Sci Process* 1998;67:385–90.
- [15] Fuhr G, Arnold WM, Hagedorn R, Muller T, Benecke W, Wagner B, et al. Levitation, holding, and rotation of cells within traps made by high-frequency fields. *Biochim Biophys Acta* 1992;1108:215–23.
- [16] Schnelle T, Hagedorn R, Fuhr G, Fiedler S, Muller T. 3-dimensional electric-field traps for manipulation of cells—calculation an experimental verification. *Biochim Biophys Acta* 1993;1157:127–40.
- [17] Voldman J, Toner M, Gray ML, Schmidt MA. Design and analysis of extruded quadrupolar dielectrophoretic traps. *J Electrstat* 2003;57:69–90.
- [18] Liu GR. Mesh free methods: moving beyond the finite element method. Boca Raton: CRC Press; 2003.
- [19] Kansa EJ. A scattered data approximation scheme with application to computational fluid dynamics. I and II *Comput Math Appl* 1990;19:127–61.
- [20] Kansa EJ. Multiquadrics—a scattered data approximation scheme with application to computational fluid dynamics. *Comput Math Appl* 1990;19(8/9):127–45.
- [21] Ding H, Shu C, Yeo KS, Xu D. Development of least-square-based two-dimensional finite-difference schemes and their application to simulate natural convection in a cavity. *Comput Fluids* 2004;33:137–54.
- [22] Chen DF, Du H, Li WH, Shu C. Numerical modeling of dielectrophoresis using a meshless approach. *J Micromech Microeng* 2005;15:1040–8.
- [23] Green NG, Ramos A, Morgan H. Numerical solution of the dielectric and traveling wave forces for interdigitated electrode arrays using the finite element method. *J Electrstat* 2002;56:235–54.

- [24] Voldman J, Gray ML, Toner M, Schmidt MA. A microfabrication-based dynamic array cytometer. *Anal Chem* 2002;74:3984–90.
- [25] Liu GR, Liu MB. Smoothed particle hydrodynamics: a meshfree particle method. Singapore: World Scientific; 2003.
- [26] Morgan H, Hughes MP, Green NG. Separation of submicron bioparticles by dielectrophoresis. *Biophys J* 1999;77:516–25.
- [27] Liu GR, Gu YT. A local radial point interpolation method (LRPIM) for free vibration analyses of 2-D solids. *J Sound Vib* 2001;246(1): 29–46.
- [28] Wang JG, Liu GR. A point interpolation meshless method based on radial basis functions. *Int J Numer Methods Eng* 2002;54: 1623–48.
- [29] Wang JG, Liu GR. On the optimal shape parameters of radial basis functions used for 2-D meshless methods. *Comput Methods Appl Mech Eng* 2002;191:2611–30.
- [30] Wang JG, Liu GR, Lin P. Numerical analysis of biot's consolidation process by radial point interpolation method. *Int J Solids Struct* 2002;39(6):1557–73.
- [31] Liu GR, Yan L, Wang JG, Gu YT. Point interpolation method based on local residual formulation using radial basis functions. *Struct Eng Mech* 2002;14(6):713–32.
- [32] Gu YT, Liu GR. A boundary radial point interpolation method (BRPIM) for 2-D structural analyses. *Struct Eng Mech* 2003;15(5): 535–50.
- [33] Liu GR, Dai KY, Lim KM, Gu YT. A radial point interpolation method for simulation of two-dimensional piezoelectric structures. *Smart Mater Struct* 2003;12:171–80.
- [34] Dai KY, Liu GR, Han X, Li Y. Inelastic analysis of 2D solids using a meshfree RPIM based on deformation theory. *Comput Methods Appl Mech Eng* 2006;195:4179–93.
- [35] Li Y, Liu GR, Luan MT, Dai KY, Zhong ZH, Li GY, Han X. Contact analysis for solids based on linearly conforming RPIM. *Comput Mech* 2006, in press.
- [36] Liu GR, Zhang GY, Dai KY, Wang YY, Zhong ZH, Li G, Han X. A linearly conforming point interpolation method (LC-PIM) for 2D solid mechanics problems. *Int J Comput Methods* 2006;2:645–65.